Baroclinic shift of hypersonic heating streaks over an ablating compression ramp

Başkaya, A. O.; Hickel, S.

DOI
10.1063/5.0281627

Publication date
2025

Document Version
Final published version

Published in
Physics of Fluids

RESEARCH ARTICLE | NOVEMBER 07 2025

Baroclinic shift of hypersonic heating streaks over an ablating compression ramp

A. O. Başkaya ; S. Hickel

Physics of Fluids 37, 116108 (2025)
https://doi.org/10.1063/5.0281627

Physics of Fluids ARTICLE pubs.aip.org/aip/pof

Baroclinic shift of hypersonic heating streaks over an ablating compression ramp

Cite as: Phys. Fluids **37**, 116108 (2025); doi: 10.1063/5.0281627
Submitted: 20 May 2025 · Accepted: 15 October 2025 ·
Published Online: 7 November 2025

A. O. Başkaya[a] and S. Hickel

AFFILIATIONS

Faculty of Aerospace Engineering, Delft University of Technology, 2629HT Delft, The Netherlands

[a]Author to whom correspondence should be addressed: a.o.baskaya@tudelft.nl

ABSTRACT

We present novel observations from direct numerical simulations of transitional Mach 8 flow over a 15° compression ramp ablator. Heating streaks over the ramp are seen to undergo a half-wavelength shift near the location of transition from laminar to turbulent boundary layer flow. This phenomenon leads to an intriguing pattern of ablation grooves on the surface. Our analysis shows that the underlying mechanism is driven by the baroclinic torque in the strongly stratified near-wall region. We discuss the impact of this *baroclinic shift* for a surface undergoing ablative recession and assess its sensitivity to different thermal boundary conditions and perturbation amplitudes.

I. INTRODUCTION

Streamwise vortices emerging from flow instabilities driven by streamline curvature and shock-wave/boundary-layer interactions are ubiquitous in high-speed flows.[1] Through the lift-up mechanism, these vortices induce spanwise variations in the flow field and especially in the surface quantities. They influence the species concentrations in a reacting boundary layer by carrying mass, the flow dynamics by transporting momentum, and the surface heat load by advecting energy. Peak heating rates and locations can be substantially altered by the formation and evolution of streamwise streaks.[2] The generation of streamwise vortices has been attributed to several different mechanisms, including convective and intrinsic instabilities,[3] which can destabilize the laminar flow and eventually trigger transition to turbulence. Of particular interest for the current work are baroclinic effects due to the interaction of strong wall-normal density gradients with transversal pressure gradients, such as the mechanism studied recently by Zapryagaev *et al.*[4] and Dwivedi *et al.*[5] on hypersonic compression ramp configurations. Developing a detailed understanding of these interactions is crucial in predicting their occurrence during the flight of high-speed aircraft and spacecraft.

Counting the aforementioned works, influential studies concerned with the formation of streamwise vortices at flow separation or reattachment are not scarce. However, often due to limitations imposed by ground-testing facilities,[6,7] previous studies considered almost exclusively (with the exception of Ref. 8) short ramp lengths of only one L, where L is the distance from the leading edge to the ramp corner.[3,9–12] Because this compact setup became canonical for fundamental research on such interactions, the downstream development of the transitional streaks may have received insufficient attention.

The specific aim of this present work is to study the influence of persistent vortex structures, their evolution, and the effect of the resulting streak pattern in the context of thermal protection systems (TPS), where the surface of the object is eroding away as a result of gas–surface interactions (GSI), including ablation. Intriguing ablation patterns, such as cross-hatching, have been observed in wind tunnel experiments as well as on recovered objects that have survived atmospheric entry.[13] The origin of these patterns and their effect on the heat load and the boundary-layer stability is a complex multi-physics problem with many unknowns and is far from being well understood. Low-temperature ablators facilitate the study of surface recession patterns in the absence of high-temperature effects, while still maintaining flight-relevant characteristics of TPS.[14] Such an ablative material, camphor, has been selected in this work to assess the streak pattern over an ablating surface. To this end, we consider a 15° compression ramp configuration exposed to Mach 8 flow and a ramp length of approximately $3L$. The focus of this paper is on the perturbation growth in the laminar boundary layer. A more detailed analysis on ablation modeling is part of a parallel work[15] and turbulence–ablation interactions are investigated in another study.[16]

This paper presents our observations of a novel phenomenon and an analysis of the underlying physical mechanisms. The setup of our computational experiments is described in Sec. II. We

report the emergence of a streamwise vortex structure that causes a characteristic shift in the heating streaks over the compression ramp in Sec. III A and explicate our physical theory and interpretation in Sec. III B. We discuss the impact of this interaction on surface ablation in Sec. III C and its sensitivity to inflow perturbation amplitudes in Sec. III D. Concluding remarks are given in Sec. IV.

II. COMPUTATIONAL SETUP AND NUMERICAL METHODS

Our numerical experiments are inspired by the works of Chuvakhov *et al.*[17] and Dwivedi *et al.*,[5] which we have previously used as one of the validation cases for the numerical methods employed in the present study (see Ref. 15). Unlike these past studies, the present study considers an extended domain approximately double the length in the streamwise direction. The compression ramp geometry consists of a flat plate with a sharp leading edge and a length of $L = 0.05$ m that is aligned with the Mach 8 free-stream flow, followed by a 15° wedge until 0.195 m in the streamwise direction, as shown in Fig. 1. The spanwise width of the domain is 0.003 m to capture one wavelength of the most unstable mode found by Dwivedi *et al.*,[5] which agrees notably well with the spacing of heating streaks observed by Chuvakhov *et al.*[17] experimentally. The freestream and inflow conditions are defined by Mach number $M_\infty = 8$, $Re_L = 3.7 \times 10^5$, pressure $p_\infty = 355$ Pa, and temperature $T_\infty = 55$ K. Top and right-most boundaries are set as non-reflecting outflow. Since experimental findings did not show any visible sign of relevant subharmonic modes, we have chosen to exclude subharmonic dynamics through periodic boundary conditions in the spanwise direction. The scope of this paper is the perturbation growth in the laminar boundary layer. The confinement effects that possibly influence the far downstream evolution of the turbulent boundary layer are thus acceptable. The domain is discretized into 254×10^6 cells, where the smallest cells at the surface have dimensions $[\Delta h_x, \Delta h_y, \Delta h_z] = [1.5 \times 10^{-5}, 3.1 \times 10^{-6}, 4.7 \times 10^{-5}]$ m. The mesh fully resolves several higher harmonics of the perturbation wavelength and is appropriate for accurate predictions of the onset of transition to turbulence. This has been verified in a grid convergence study. Figure 2 shows the agreement between the grid-converged laminar solution and the reference results from Dwivedi *et al.*[5] Note that the reference results are only available until $1.9L$.

Three boundary conditions are studied for the ramp surface: (1) an inert adiabatic wall, (2) an inert isothermal wall with a temperature of $T_w = 293$ K, and (3) a reactive ablative wall where an energy balance is solved for the wall temperature varying along the ramp. These correspond to Eckert numbers of $Ec = 3.96$ for the isothermal wall and range between $Ec = [3.91, 4.55]$ for the ablative wall, where the Eckert number is

$$Ec = \frac{u_\infty^2}{c_p(T_r - T_w)}, \tag{1}$$

with the freestream velocity $u_\infty = 1190$ m/s, and the specific heat at constant pressure $c_p = 1003$ J/(kg K). The recovery temperature T_r was calculated by assuming a recovery factor of 0.846 based on the adiabatic wall temperature predictions. For the simulations with an ablative wall, instead of a rigid wedge, we take the solid material to be camphor, a low-temperature ablator naturally undergoing sublimation, $C_{10}H_{16}O_{(solid)} \rightarrow C_{10}H_{16}O_{(gas)}$, at the present conditions.

We solve the compressible Navier–Stokes equations for a multispecies chemically inert fluid

$$\partial_t \boldsymbol{U} + \nabla \cdot \boldsymbol{F}(\boldsymbol{U}) = \boldsymbol{S}, \tag{2}$$

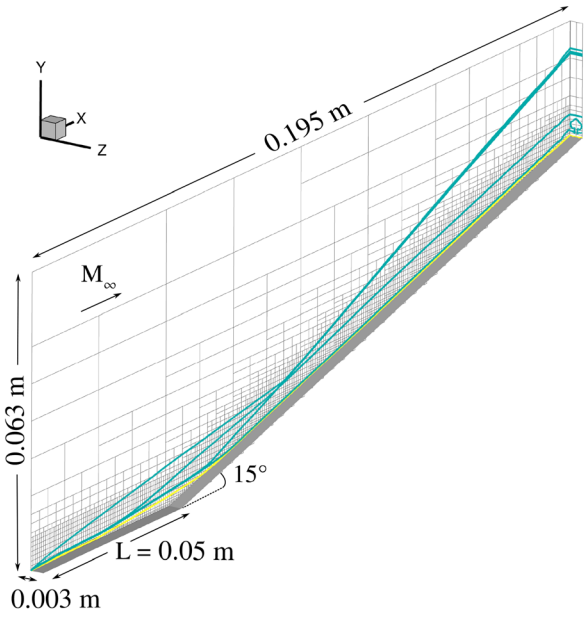

FIG. 1. Sketch of the compression ramp geometry with the block structure of the Cartesian AMR grid. Mach number contours are plotted with blue lines, and the sonic line is highlighted in yellow.

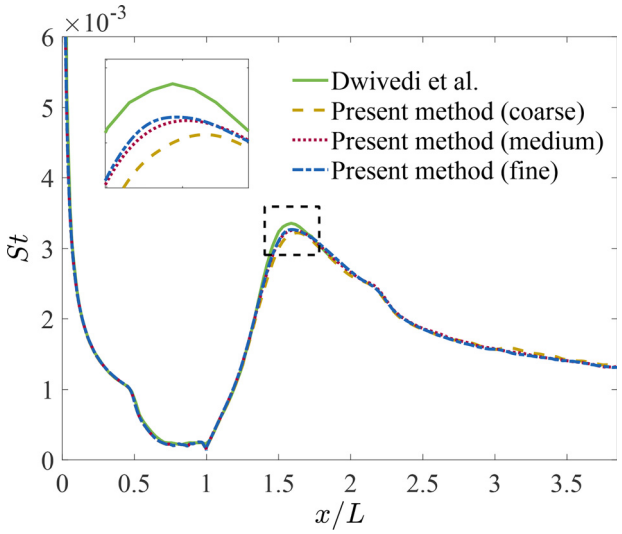

FIG. 2. Comparison of Stanton numbers obtained using the present methodology with successively refined numerical grids. Reference results are taken from Dwivedi *et al.*[5]

where $\boldsymbol{U} = [\rho_i, \rho u, \rho v, \rho w, \rho E]^{\mathrm{T}}$ is the vector of conserved variables, $\boldsymbol{F} = \boldsymbol{F}_{inv} + \boldsymbol{F}_{vis}$ is the sum of inviscid and viscous fluxes, and $\boldsymbol{S}$ is the vector of source terms. Along the x-axis, these fluxes are

$$\boldsymbol{F}_{inv} = \begin{bmatrix} \rho_i u \\ \rho u^2 + p \\ \rho uv \\ \rho uw \\ u(\rho E + p) \end{bmatrix}, \quad \boldsymbol{F}_{vis} = \begin{bmatrix} J_{\mathrm{x},i} \\ -\tau_{\mathrm{xx}} \\ -\tau_{\mathrm{xy}} \\ -\tau_{\mathrm{xz}} \\ -(\tau_{\mathrm{xx}} u + \tau_{\mathrm{xy}} v + \tau_{\mathrm{xz}} w) + q_{\mathrm{x}} \end{bmatrix}, \tag{3}$$

where ρ_i is the species partial density for the i^{th} species, $\boldsymbol{u}$ is the mixture average velocity, ρ is the mixture density, p is the mixture pressure, and $E = e + u^2/2$ is the specific total energy, which is the sum of the thermodynamic internal energy e and the kinetic energy. Note that the species source terms in $\boldsymbol{S}$ are non-zero only at the ablating surface as no homogeneous gas-phase reactions are occurring at the conditions studied in this work. Modeling approaches for the species diffusion flux $\boldsymbol{J}_i$, the viscous stress tensor $\boldsymbol{\tau}$, and the total heat flux $\boldsymbol{q}$ are detailed in Baskaya *et al.*[15] Single species air is used for the simulations with an inert wall. Air is modeled by Sutherlands' law for the viscosity, specific heats are taken from NASA polynomials,[18] and thermal conductivity is obtained from a Prandtl number of 0.72. For camphor gas, introduced due to the ablative boundary condition, cubic polynomials for viscosity and thermal conductivity from Zibitsker *et al.*[19] are used. Diffusivity is calculated based on the model of Haskins reported in that same work. Wilke's mixing rule is used for the air-camphor mixture properties.

The governing equations are solved with our in-house solver, INCA (https://inca.cfd), which is a high-fidelity finite-volume solver for direct numerical simulations (DNS) and large eddy simulations (LES) of the compressible chemically reacting Navier–Stokes equations and provides a large number of different discretization schemes on three-dimensional block-Cartesian grids with adaptive mesh refinement (AMR) (see, e.g., Ref. 20). For the purposes of this research, a third-order weighted essentially non-oscillatory (WENO) scheme[21] with HLLC flux function[22] is selected for the hyperbolic flux. Second-order centered differences are used for the viscous terms and the explicit third-order Runge–Kutta scheme of Gottlieb and Shu[23] is chosen for time integration. The ramp wall is represented by a cut-element immersed boundary method,[24] which is a consistent and conservative extension of the finite-volume flux balance for mesh cells being split by interfaces. Boundary conditions are imposed on the cut-elements that result from the intersection of the Cartesian fluid grid and the surface triangulation of the solid. Details of the numerical schemes and the extension of the cut-element method to reacting surfaces are presented by Baskaya *et al.*[25]

We follow the GSI methodology described by Bianchi *et al.*[26] for simulations involving camphor ablation. For the ablative boundary condition, mass and energy balances are solved at the surface, taking into account sublimation, diffusion, and blowing. We solve for the mass blowing rate $\dot{m} = \sum_i \dot{\omega}_{i,w}$, calculated as the sum of the species source terms $\dot{\omega}_{i,w}$. The chemical source term for camphor is given by

$$\dot{\omega}_{c,w} = \alpha \rho (p_v - p_c) \sqrt{\frac{M_c}{2\pi R_u T_w}}, \tag{4}$$

where α is the empirical vaporization coefficient, p_v and p_c are the vapor and partial pressures of camphor, respectively, M_c is the molecular weight of camphor, and R_u is the universal gas constant.[19] Vapor pressure and material properties for camphor are taken from Rotondi *et al.*[14] The speed at which ablation products blow out of the surface is then expressed as $v_b = \dot{m}/\sum_i \rho_{i,w}$.

Values obtained for species densities and mass blowing speeds are imposed as boundary conditions for the Navier–Stokes equations. Similarly, the surface recesses at a speed of $v_s = \dot{m}/\rho_s$, where $\rho_s = 990\,\mathrm{kg/m^3}$ is the density of solid camphor.[14] The surface recession is orders of magnitude slower than the characteristic time scales of the fluid flow. To achieve a sufficient amount of shape change within a reasonable wall-clock time, it is common practice in simulations with ablative recession to accelerate the geometry change. We have found that an accurate representation of physicochemistry and fluid dynamics is ensured with an acceleration factor of 10^4.

The source term $\boldsymbol{S}$ includes a local forcing applied to the vertical-momentum equation between $x_1 = 0.02\,\mathrm{m}$ and $x_2 = 0.023\,\mathrm{m}$ (measured from the sharp leading edge) to perturb the laminar base flow:

$$S(x, y, z) = A_s f(x) \exp\left(-\left[\frac{y - y_0}{\sigma}\right]^2\right) \sin\left(\frac{2\pi z}{\lambda_z}\right), \tag{5}$$

where $y_0 = 0.5$ mm, $\sigma = 0.3$ mm, and $\lambda_z = 3.0$ mm following Baskaya *et al.*[15] The shape function in the streamwise direction is

$$f(x) = \begin{cases} 0.0, & x < x_1 \text{ or } x > x_2, \\ \left(\tilde{x}(2r_x - \tilde{x})/r_x^2\right)^3, & \tilde{x} < r_x, \\ 1.0, & \text{otherwise}, \end{cases} \tag{6}$$

where $\tilde{x} = \min(|x - x_1|, |x - x_2|)$ and $r_x = \frac{1}{4}(x_2 - x_1)$. The amplitude is $A_s = 10^5\,\mathrm{kg/m^2 s^2}$ unless stated otherwise.

For ablative walls, the GSI boundary condition additionally introduces source terms $\dot{\omega}_{i,w}$ for mass conservation, $\dot{m}(\boldsymbol{v}_b \cdot \boldsymbol{n})$ with the surface normal vector $\boldsymbol{n}$ for momentum conservation, and $\dot{m}\left(h + \frac{1}{2}\|\boldsymbol{v}_b\|^2\right)$ with mixture enthalpy h for energy conservation.

III. ANALYSIS OF THE *BAROCLINIC SHIFT*

A. Observations

Our analysis begins by observing the vortex formation visualized in Fig. 3, where the domain is duplicated in the spanwise direction to enhance visual intuition. Initial perturbations develop into a steady streamwise vortex-streak system. The counter-rotating vortices grow to a significant amplitude as the flow reattaches on the ramp and evolve further as they travel downstream. Formation of secondary vortices surrounding the streaks signals the onset of transition and the eventual turbulent breakdown.

The lift-up effect results in alternating hotter and colder streaks along the ramp's surface, as shown in Fig. 4(a) for the case with an inert isothermal wall. These thermal streaks are most discernible downstream of the reattachment point near $x = 0.08$ m, where $x = 0.05$ m is the corner of the ramp. An intriguing observation can be made from these near-wall streak patterns. Traveling downstream over the ramp, the streak pattern undergoes an abrupt variation: hidden underneath the vortical structures in Fig. 3, the regions of heating and cooling interchange near $x = 0.13$ m, indicated by arrows in Fig. 4. This shift is more clearly noticeable in the contour plot in Fig. 4(b),

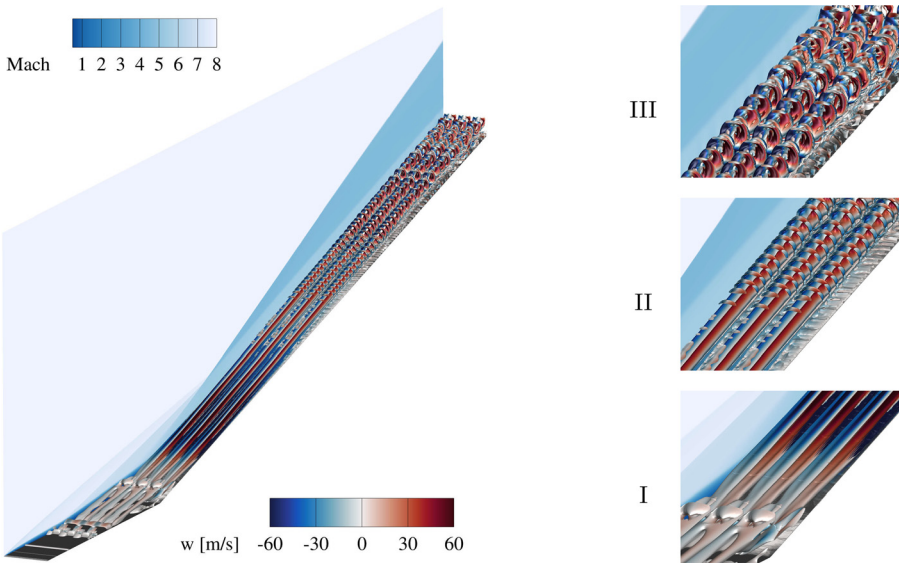

FIG. 3. Isometric view of the domain with a Q-criterion iso-surface contoured with the spanwise velocity. The spanwise background shows Mach number contours. Three close-up views on the right-hand side focus on (I) the steady streaks reattaching on the ramp surface, (II) the onset of transition, and (III) the turbulent breakdown. Domain is periodically extended in the spanwise direction for visualization.

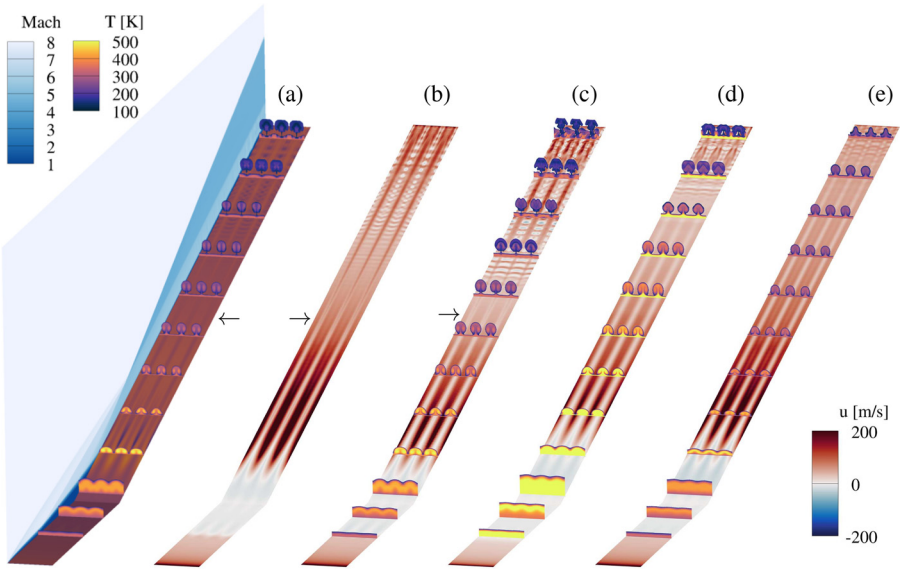

FIG. 4. Isometric view of the spatial evolution of streak patterns over (a), (b), and (e) an inert isothermal wall, (c) an ablative wall (see Sec. III C), and (d) an inert adiabatic wall with (a)–(d) high amplitude and (e) low amplitude perturbations (see Sec. III D). Streamwise slices show temperature. The ramp surface is contoured by (a) temperature and (b)–(e) streamwise velocity. Arrow markers indicate locations of baroclinic shift.

which shows the streamwise velocity at a wall distance of 20 μm for the same case. Beyond the shift location, velocity deficit streaks become velocity excess streaks. This suggests the existence of a vortex pair close to the wall with a phase shift of 180° compared to the vortex orientations near reattachment. We will refer to this point where the streaks seemingly "reverse" as the location of *baroclinic shift*, since we believe that this shift is caused by baroclinic effects as the rest of this discussion will elucidate. Furthermore, as suggested by the snapshots of different configurations in Fig. 4, we will also remark that this shift is not observed with an inert adiabatic wall [Fig. 4(d)] or with lower amplitude perturbations [Fig. 4(e)], but it has the most severe implications on a wall that undergoes ablative recession [see Fig. 4(c)].

To aid the investigation, we present contours of the spanwise velocity, temperature, and density distributions on streamwise slices at $x = [0.0647, 0.0868, 0.1089, 0.1311]$ m in Fig. 5 for the case with an inert isothermal wall. These four slices are located between reattachment and the baroclinic shift. The reattachment location can be identified from the Mach number contours in Fig. 4(a). The baroclinic shift location is indicated by an arrow in the same figure. We can immediately distinguish a vortex structure in the first (leftmost) slice of spanwise velocity contours. The over-saturated colormap is selected in such a way as to discern the smallest and weakest occurrences. In the second slice, we can already see the emergence of a secondary vortex near the surface. In subsequent slices, this secondary vortex grows and evolves. What we observe in these slices directly reflects the shift in the wall pattern in Fig. 4(b). Comparing the first and the last slices, we observe the formation of a secondary vortex pair close to the wall with the

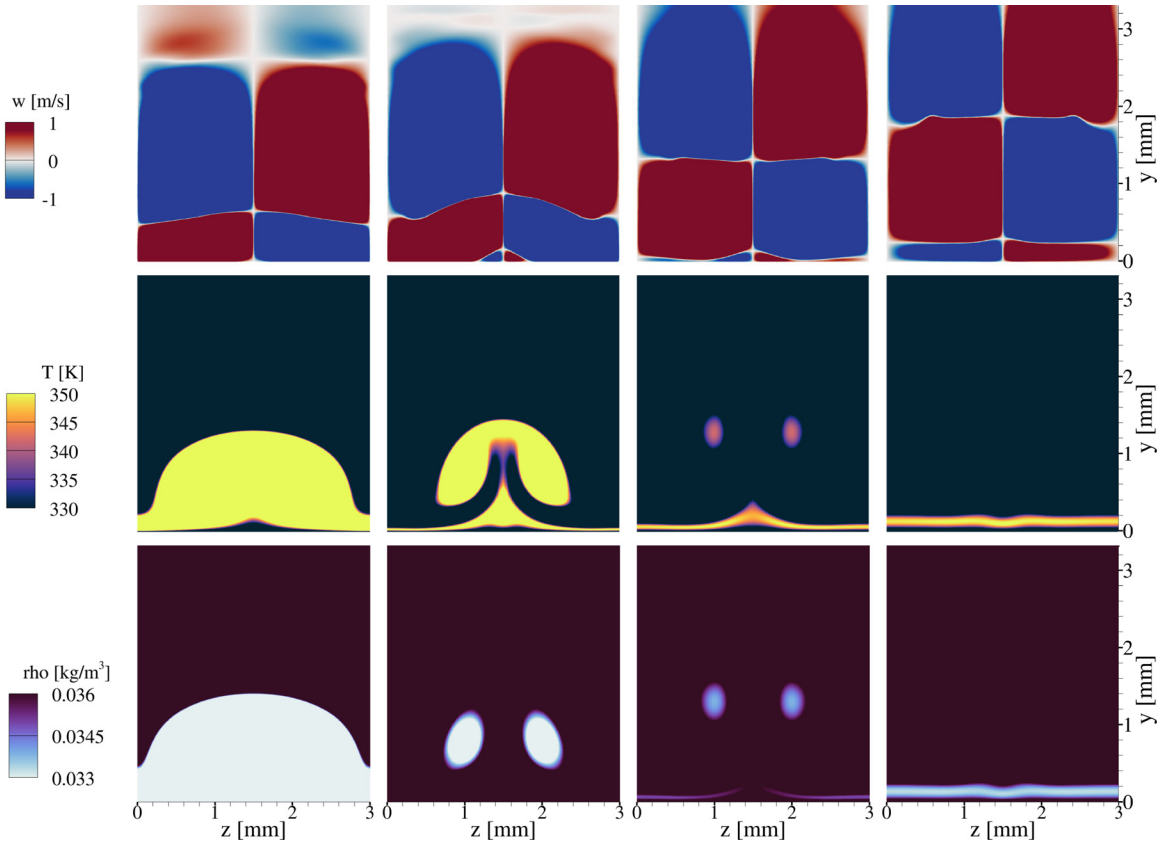

FIG. 5. Streamwise slices along the ramp at $x = [0.0647, 0.0868, 0.1089, 0.1311]$ m plotting spanwise velocity, temperature, and density variations. Horizontal axis is the spanwise direction. Flow direction is pointing inward.

opposite sense of rotation. These secondary perturbation vortices are counteracting the lift-up effect of the primary perturbation.

B. Physical interpretation

To understand the mechanism that causes this phenomenon, let us examine the other quantities in Fig. 5. The temperature distributions clearly show the "mushroom" structure generated by the lift-up effect. Hot gas is ejected away from the wall by these vortices. Following the slices downstream, we see that the flow gradually cools down. This happens rapidly for the vortices away from the wall as the lift-up effect promotes mixing with the cold freestream. The cold wall influences the flow in a similar manner. As a result, at a certain downstream distance, only a thin region with higher temperatures remains between two colder layers, trapped between the surface and the outer flow. This *trapped* flow remains hot due to viscous dissipation of kinetic energy. The fluid density is significantly lower in this region as can be seen from the slices of density variations in Fig. 5. A critical observation is that the sign of the wall-normal density gradient reverses in this region.

Figure 6 focusses on the region near the surface and shows the density variations for the slice at $x = 0.1311$ m, corresponding to the last (rightmost) slice in Fig. 5. The spanwise range is extended to include one more streak for visualization purposes. In the topmost contour plot, pressure iso-lines (white) are overlaid on density contour fields. In the contour plots below, black lines represent density iso-lines. We can observe the variations in density and pressure from the first two slices. It is clear that these variations lead to a density gradient $\nabla\rho$ in the wall-normal direction and a pressure gradient ∇p in the spanwise direction. The misalignment of these two gradients gives rise to baroclinic torque $T_b = \nabla\rho \times \nabla p$. This vorticity production term, T_b/ρ^2, is plotted in the same figure. Streamwise vorticity is also included to show that this component has the same sign as the baroclinic term. Observe that the thin region of lower density (the trapped flow) that we have identified earlier leads to a density gradient in the direction pointing away from the surface above a certain height and in the opposite direction near the wall. With the pressure-gradient direction remaining the same through the thin region, the baroclinic torque has the opposite direction above and below the trapped flow. The effect of this can also be seen when we look at the evolution of baroclinic torque and streamwise vorticity in Fig. 7 at the same locations shown in Fig. 5. In the first slice, the primary streaks are promoted by the baroclinic torque. In the following slices, the baroclinic term near the wall feeds emerging vortices with the opposite sense of rotation. The baroclinic torque opposes the preexisting streamwise vortices and produces streamwise vorticity with opposite sign prior to the onset of transition.

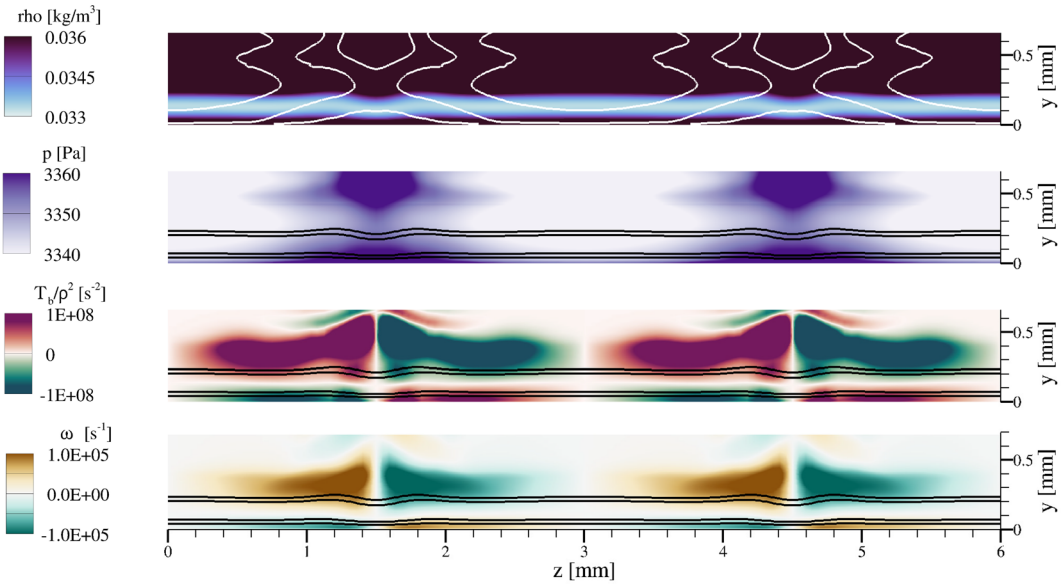

FIG. 6. Streamwise slice at $x = 0.1311$ m showing density, pressure, baroclinic torque, and vorticity distributions. Pressure contour lines are plotted in white, and density contour lines are plotted in black. Horizontal axis is the spanwise direction. Flow direction is pointing inward.

This confirms that the baroclinic torque is the mechanism that generates the alternating streak patterns shown in Fig. 4.

Since the Eckert numbers predicted for the inert isothermal [Fig. 4(b)] and the ablative wall [Fig. 4(c)] are similar, i.e., both have significantly colder wall temperatures compared to post-shock temperatures, both cases have similar stratification followed by a baroclinic shift. The onset of this effect is at a similar location between the two conditions; however, because ablation further destabilizes the flow as observed by Baskaya *et al.*,[15] the newly emerged near-wall streaks persist for a shorter length downstream before starting to break down. On the other hand, since the reversal in the baroclinic torque strongly depends on the existence of the stratified thermal layer near the wall, this effect is absent in Fig. 4(d) for the inert adiabatic wall. No clear streak reversal can be observed before the laminar flow starts to break down near the end of the ramp.

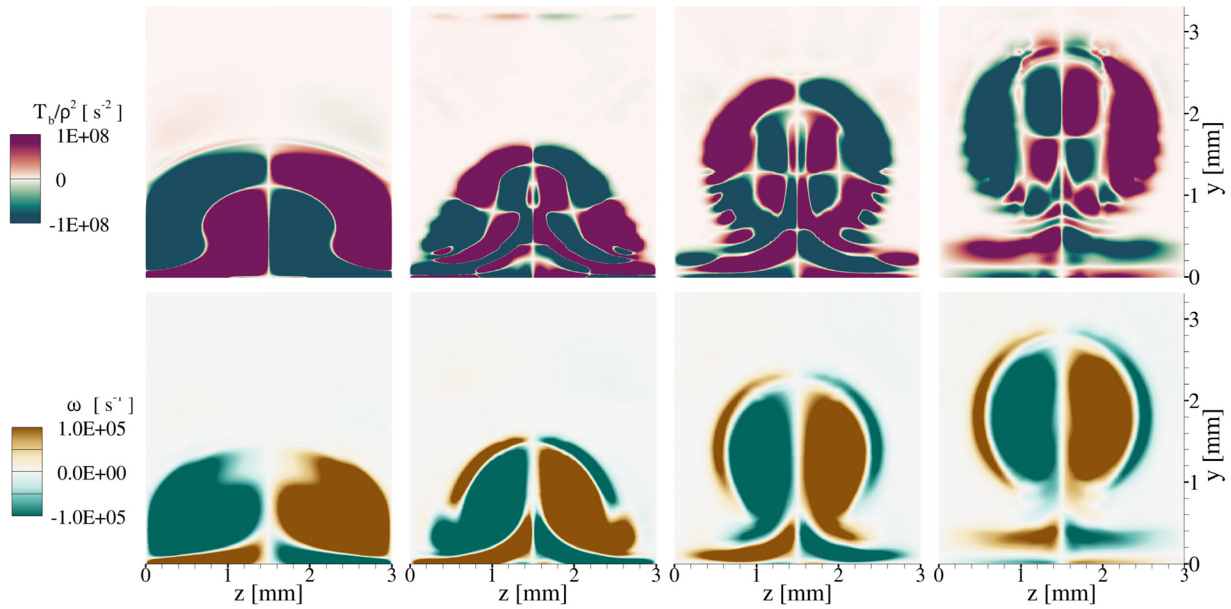

FIG. 7. Streamwise slices along the ramp at $x = [0.06474, 0.08684, 0.1089, 0.1311]$ m showing baroclinic torque and vorticity variations. Horizontal axis is the spanwise direction. Flow direction is pointing inward.

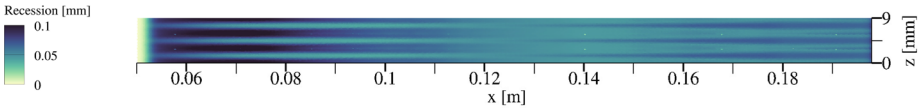

FIG. 8. Recession pattern over the ablative ramp. Darker regions signify deeper grooves in the eroding surface material.

C. Impact on surface ablation

The shift in intense surface heating locations has severe consequences for applications with ablative surface materials. For our numerical experiments, we employ camphor, which sublimates at the considered flow conditions. Ablation thus introduces camphor blowing out of the ramp as the surface erodes.

Figure 8 shows a top-down view of the ablated ramp surface after a maximum of 0.1 mm of recession. Immediately downstream of reattachment, we can clearly distinguish how different rates of sublimation have created spanwise variations in recession. As higher temperatures increase sublimation rates, deeper grooves formed by recession align with the heating streaks. Farther downstream, beyond the baroclinic shift, the recession pattern is reversed as the secondary vortices emerge from the wall. The resulting recession pattern reflects the trend we have observed in Fig. 4(a).

Figure 9 shows the instantaneous streamwise distributions of mass blowing rates, $\dot{m}$, and Stanton numbers

$$St = \frac{q_w}{\rho_\infty U_\infty c_p (T_r - T_w)}, \tag{7}$$

at $z = 1.5$ mm and $z = 0.0$ mm. Note that $z = 1.5$ mm corresponds to the center of the lift-up effect of the primary perturbation. Both quantities follow a similar profile as higher heat fluxes lead to higher mass blowing rates and, therefore, higher recession rates. In Fig. 9, their values along $z = 0.0$ mm are initially larger than those along $z = 1.5$ mm; however, this difference reduces downstream until the higher value interchanges. The intersection of these two lines gives an indication of the shift location. The fluctuations observed for $x > 0.15$ m relate to the growth of unsteady perturbations as the flow destabilizes and eventually transitions to turbulence downstream. The downstream fluctuations are more apparent in Fig. 9(b) since the heat fluxes are more sensitive to flow instabilities. Laminar to turbulent transition is not further addressed in this paper as it is the subject of an ongoing collaboration with a research group at the University of Maryland.[15]

D. Sensitivity to perturbation amplitude

To assess the sensitivity of the results to the perturbation amplitudes, we have performed the same inert isothermal wall simulations with 30% of the forcing amplitude used in the preceding cases. The resulting near-surface velocities with low-amplitude perturbations are presented in Fig. 4(e). The low-amplitude case does not show the reversal of the near-wall streaks. With a lower initial perturbation, reattachment and the resulting streaks occur farther downstream as can be deduced from the expanded recirculation region. The lift-up effect and the baroclinic torque are weaker compared to the high-amplitude case.

We compare the Stanton numbers for high and low amplitude cases in Fig. 10. For the high-amplitude case, we clearly see how the values along alternating streaks intersect, whereas this does not occur for the low amplitude case before the laminar streak pattern begins to destabilize. The ablative (see Fig. 9) and the isothermal-wall simulations with high amplitude perturbations show similar trends: an initial peak is followed by a stronger second peak downstream of the transition location. The low-amplitude case shows only weak secondary growth within the current domain.

IV. CONCLUSIONS AND REMARKS

We have presented novel observations of intriguing heating and ablation patterns over a compression ramp at Mach 8. We found that the dominant physical mechanism behind this phenomenon is the baroclinic torque near the cooled surface, which opposes the streamwise vorticity of the primary perturbation. This baroclinic vorticity production is due to a layer of hot low-density fluid being trapped in the boundary layer between colder and denser fluid layers, and the spanwise pressure gradient imposed by primary streamwise-vortex perturbations

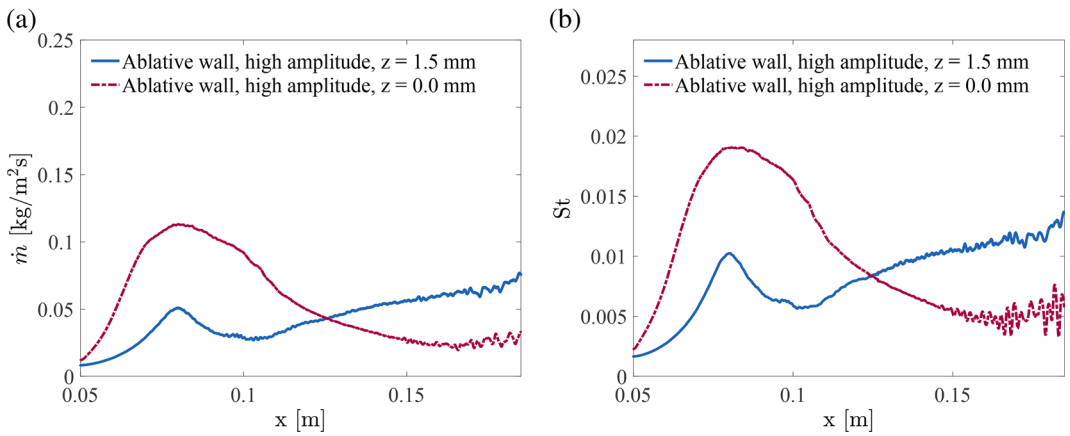

FIG. 9. Instantaneous streamwise distributions of (a) mass blowing rate and (b) Stanton number over the ablative wall at $z = 1.5$ mm and $z = 0.0$ mm for high amplitude perturbations.

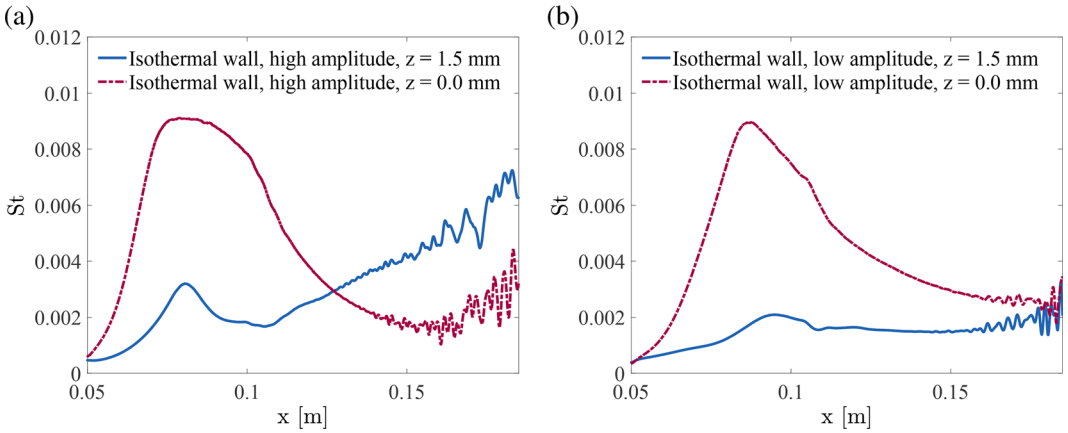

FIG. 10. Instantaneous streamwise distributions of Stanton number at $z = 1.5$ mm and $z = 0.0$ mm for (a) high and (b) low amplitude perturbations.

with sufficiently high amplitude. Secondary streamwise-vortex perturbations induced by the baroclinic torque near the wall counteract the lift-up effect of the primary perturbation, and the surface heat flux and ablation pattern shifts. This *baroclinic shift* has severe implications on gas-surface interactions as it drastically changes the distribution of species concentrations and heat fluxes. We have no reason to believe that this phenomenon is restricted to ramp geometries; diabatic cold walls and strong perturbations are among the most important conditions. The same or a similar mechanism could play a role in the formation of more complex ablation patterns.

ACKNOWLEDGMENTS

The authors extend their heartfelt gratitude to Professor Christoph Brehm and Sean Dungan of the University of Maryland for their invaluable collaboration on the setup and methodology and acknowledge support of the Dutch Research Council (NWO) through project no. 2023.028 and the SURF Cooperative for providing access to Snellius.

AUTHOR DECLARATIONS

Conflict of Interest

The authors have no conflicts to disclose.

Author Contributions

A. O. Baskaya: Conceptualization (equal); Data curation (equal); Formal analysis (equal); Investigation (equal); Methodology (equal); Software (equal); Validation (equal); Visualization (equal); Writing – original draft (equal); Writing – review & editing (equal). **S. Hickel:** Conceptualization (equal); Funding acquisition (equal); Methodology (equal); Project administration (equal); Software (equal); Supervision (equal); Writing – review & editing (equal).

DATA AVAILABILITY

The data that support the findings of this study are available from the corresponding author upon reasonable request.

REFERENCES

[1]N. Sandham, E. Schülein, A. Wagner, S. Willems, and J. Steelant, "Transitional shock-wave/boundary-layer interactions in hypersonic flow," J. Fluid Mech. **752**, 349–382 (2014).
[2]D. S. Dolling, "Fifty years of shock-wave/boundary-layer interaction research: What next?," AIAA J. **39**, 1517–1531 (2001).
[3]S. Cao, J. Hao, I. Klioutchnikov, C.-Y. Wen, H. Olivier, and K. A. Heufer, "Transition to turbulence in hypersonic flow over a compression ramp due to intrinsic instability," J. Fluid Mech. **941**, A8 (2022).
[4]V. Zapryagaev, I. Kavun, and I. Lipatov, "Supersonic laminar separated flow structure at a ramp for a free-stream Mach number of 6," Prog. Flight Phys. **5**, 349–362 (2013).
[5]A. Dwivedi, G. S. Sidharth, J. W. Nichols, G. V. Candler, and M. R. Jovanović, "Reattachment streaks in hypersonic compression ramp flow: An input-output analysis," J. Fluid Mech. **880**, 113–135 (2019).
[6]G. Simeonides and W. Haase, "Experimental and computational investigations of hypersonic flow about compression ramps," J. Fluid Mech. **283**, 17–42 (1995).
[7]A. Roghelia, H. Olivier, I. Egorov, and P. Chuvakhov, "Experimental investigation of Görtler vortices in hypersonic ramp flows," Exp. Fluids **58**, 139 (2017).
[8]I. Egorov, V. Neiland, and V. Shredchenko, "Three-dimensional flow structures at supersonic flow over the compression ramp," AIAA Paper No. 2011-730 (2011).
[9]S. Navarro-Martinez and O. Tutty, "Numerical simulation of Görtler vortices in hypersonic compression ramps," Computers Fluids **34**, 225–247 (2005).
[10]Y. Zhuang, H.-J. Tan, Y.-Z. Liu, Y.-C. Zhang, and Y. Ling, "High resolution visualization of Görtler-like vortices in supersonic compression ramp flow," J. Vis. **20**, 505–508 (2017).
[11]M. Lugrin, S. Beneddine, C. Leclercq, E. Garnier, and R. Bur, "Transition scenario in hypersonic axisymmetrical compression ramp flow," J. Fluid Mech. **907**, A6 (2021).
[12]M. Marini, "Analysis of hypersonic compression ramp laminar flows under sharp leading edge conditions," Aerosp. Sci. Technol. **5**, 257–271 (2001).
[13]S. W. Stock, "Surface patterns on subliming and liquefing ablation materials," AIAA J. **13**, 1217–1223 (1975).
[14]M. Rotondi, M. T. Migliorino, D. Bianchi, P. Pagani, and A. Turchi, "Numerical assessment of camphor ablation flight relevance in hypersonic wind-tunnel testing," J. Spacecr. Rockets **59**, 1574–1591 (2022).
[15]A. O. Başkaya, S. Hickel, S. D. Dungan, and C. Brehm, "Fluid ablation interactions on a compression ramp at Mach 8," AIAA Paper No. 2024-0501 (2024).
[16]A. Başkaya, L. Laguarda, and S. Hickel, "Turbulent hypersonic flow over a recessing low-temperature ablator," in Proceedings of the 15th International ERCOFTAC Symposium on Engineering Turbulence Modelling and Measurements (ETMM15) (2025), pp. 801–806.

[17]P. V. Chuvakhov, V. Y. Borovoy, I. V. Egorov, V. N. Radchenko, H. Olivier, and A. Roghelia, "Effect of small bluntness on formation of Görtler vortices in a supersonic compression corner flow," J. Appl. Mech. Technol. Phys. **58**, 975–989 (2017).
[18]B. J. McBride, *NASA Glenn Coefficients for Calculating Thermodynamic Properties of Individual Species* (National Aeronautics and Space Administration, John H. Glenn Research Center, 2002).
[19]A. L. Zibitsker, J. A. McQuaid, C. Brehm, and A. Martin, "Validation and analysis of a coupled fluid-ablation framework for modeling low-temperature ablator," Int. J. Heat Mass Transfer **218**, 124728 (2024).
[20]S. Hickel, C. P. Egerer, and J. Larsson, "Subgrid-scale modeling for implicit large eddy simulation of compressible flows and shock-turbulence interaction," Phys. Fluids **26**, 106101 (2014).
[21]G.-S. Jiang and C.-W. Shu, "Efficient implementation of weighted ENO schemes," J. Comput. Phys. **126**, 202–228 (1996).
[22]E. F. Toro, *Riemann Solvers and Numerical Methods for Fluid Dynamics: A Practical Introduction* (Springer-Verlag, Berlin, 2013).
[23]S. Gottlieb and C.-W. Shu, "Total variation diminishing Runge-Kutta schemes," Math. Comput. **67**, 73–85 (1998).
[24]F. Örley, V. Pasquariello, S. Hickel, and N. A. Adams, "Cut-element based immersed boundary method for moving geometries in compressible liquid flows with cavitation," J. Comput. Phys. **283**, 1–22 (2015).
[25]A. O. Başkaya, M. Capriati, A. Turchi, T. Magin, and S. Hickel, "Assessment of immersed boundary methods for hypersonic flows with gas-surface interactions," Computers Fluids **270**, 106134 (2024).
[26]D. Bianchi, M. T. Migliorino, M. Rotondi, and A. Turchi, "Numerical analysis and wind tunnel validation of low-temperature ablators undergoing shape change," Int. J. Heat Mass Transfer **177**, 121430 (2021).